

Photogrammetry Analysis of a Hypersonic Inflatable Aerodynamic Decelerator Structural Test Article



AE8900 MS Special Problems Report
Space Systems Design Lab (SSDL)
Guggenheim School of Aerospace Engineering
Georgia Institute of Technology
Atlanta, GA

Author:
Lin Li

Advisor:
Dr. Robert D. Braun

July 11, 2013

Photogrammetry Analysis of a Hypersonic Inflatable Aerodynamic Decelerator Structural Test Article

Lin Li¹ and Robert D. Braun²
Georgia Institute of Technology, Atlanta, GA, 30332

and

Alan M. Cassell³
NASA Ames Research Center, Moffett Field, CA

Analysis was performed on photogrammetry data of a 6m Hypersonic Inflatable Aerodynamic Decelerator (HIAD), an inflatable stacked torus used to aid in atmospheric entry, to understand its structural dynamics. Photogrammetry data was obtained during wind tunnel testing under various loading conditions. Test parameters included the freestream dynamic pressure, yaw angle and internal inflation pressure. In addition, two HIAD configurations were analyzed, the basic stacked torus (Baseline configuration) and a second configuration adding a torus near the shoulder to aid in rigidity (Tri-Tori configuration). The analysis includes estimating the deflection of the HIAD under loading as well as calculating the standard deviation relative to the mean deflection and the frequency content of the dynamic response. Under load, the deflection angle for each configuration ranged from 1° to 3° (1 σ). Analysis of the results indicates that the Tri-Tori configuration did not demonstrate significant benefit over the Baseline. The photogrammetry data showed that the oscillatory motion increased with higher dynamic pressure but was insensitive to yaw angle. In addition, the analysis showed that the standard deviation of the HIAD shape with respect to the average deflection increased while moving radially outwards. However, the standard deviation values calculated from different camera pairs were inconsistent and did not produce the same standard deviations especially at the interface region. The frequency analysis showed that each radial member behaved similarly to a rigid oscillator, having the same frequency content of motion along each radial direction and increased amplitude when moving radially outward. Both the frequency and shape standard deviation analyses showed that the motion of the HIAD was piecewise continuous in the azimuthal direction. These discontinuities likely arose when stitching together the images from different camera pairs. The photogrammetry data is a valuable dataset providing insight into the static and dynamic response of the HIAD under loading. However, inconsistencies in the camera imaging and stitching need to be resolved and higher temporal resolution will improve the fidelity of analysis.

¹ Graduate Research Assistant, School of Aerospace Engineering, lli313@gatech.edu

² David and Andrew Lewis Professor of Space Technology, School of Aerospace Engineering, robert.braun@aerospace.gatech.edu

³ Aerospace Engineer, alan.m.cassell@nasa.gov

Nomenclature

<i>I</i>	Inflation setting
<i>N</i>	Number of frames
<i>T</i>	Torus
<i>x</i>	x-coordinate
<i>y</i>	y-coordinate
<i>z</i>	z-coordinate

Subscripts

<i>l-8</i>	Tori number (increasing from nose to shoulder)
<i>ave</i>	Average over multiple frames
<i>i</i>	<i>i</i> th frame

Acronyms

EDL	Entry, Descent and Landing
DGB	Disk-Gap-Band
HIAD	Hypersonic Inflatable Aerodynamic Decelerator
IAD	Inflatable Aerodynamic Decelerator
IRVE	Inflatable Reentry Vehicle Experiment
MSL	Mars Science Laboratory
SIAD	Supersonic Inflatable Aerodynamic Decelerator
TPS	Thermal Protection System

I. Introduction

One of the most technically challenging aspects of planetary exploration is designing a vehicle that can execute and survive the Entry, Descent and Landing (EDL) phase of the mission. Special care has to be taken so that the entry vehicle can decelerate sufficiently as well as dissipate the large heat load experienced from traveling through the atmosphere during the entry phase.¹ This is typically accomplished using a rigid aeroshell and supersonic parachute system, qualified in the 1960's and 1970's for the Mars Viking mission. Future NASA goals include heavier robotic and eventually human-class missions to other planets, which require larger drag devices to decelerate and safely land the vehicles. This can be achieved either by increasing the diameter of the aeroshell, using a larger parachute, or developing a different EDL system.

Increasing the diameter of the aeroshell is not achievable since they need to first be packaged in the rocket payload shroud, limiting the entry vehicle maximum diameter to 5m². As a result, aeroshells are unable to scale to the size needed to safely land the requisite mass for human Mars exploration. An alternative solution is to increase drag from the aerodynamic decelerator. The most common aerodynamic decelerators have historically been parachute systems³. Parachutes have flown on every US manned mission including Apollo, which used both high altitude drogue parachutes for stabilization and main parachutes to achieve a safe terminal velocity⁴⁻⁶. However, complications in supersonic parachute inflation and their inability to survive the extreme hypersonic heating conditions place substantial limitations on parachute's abilities to land heavy payloads. As a result, the maximum deliverable payload mass to the Mars surface using a parachute system is estimated to be on the order of a few metric tons (mT). In particular, the recent successful landing of the Mars Science Laboratory (MSL) has already pushed the limit of what is achievable through reliance on incremental advances of the foundational heritage Viking technology⁷. In order to land more massive payloads on Mars and, specifically, to enable future human missions to Mars, a new, innovative technology is required.

One of the proposed EDL technologies is the Hypersonic Inflatable Aerodynamic Decelerator (HIAD). HIADs are of interest for this mission class because such devices inflate to their full size in space and are not directly constrained by the launch vehicle payload shroud diameter as are rigid aeroshells nor inflation conditions like parachutes. They can provide both deceleration and thermal protection capabilities throughout EDL, which would potentially decrease the entry vehicle complexity, providing a more reliable and efficient way to deliver payloads onto the surface of a planet. Another benefit is that HIADs can be deployed either exo-atmospherically or during the hypersonic phase of flight which allows for increased timeline before touch-down, higher landed entry mass or higher landing elevation.

HIAD development was first conducted in parallel with Supersonic Inflatable Aerodynamic Decelerators (SIAD), another type of Inflatable Aerodynamic Decelerator (IAD) that is inflated supersonically⁸. The development of IADs in the United States started as early as the 1960's when Robert W. Lenard from NASA Langley Research Center proposed the inflatable reentry glider for manned reentry from orbital flight⁹. Since then, different IAD configurations have been studied and tested, such as Isotensoids, Torus, and Tension Cones both for use as trailing IADs as well as attached IADs¹⁰⁻¹⁹. One of the most successful and widely used IAD concepts was the Ballute, developed by Goodyear Aerospace Corporation²⁰. From the mid 1970's through the mid 1990's, IAD development stagnated since Disk-Gap-Band (DGB) parachutes were fully capable for space missions at the time. Starting in 1995, interest in the development of IADs has been revisited as recently proposed missions to Mars, Titan, and Neptune could not be achieved with the DGB parachute²¹. These missions required a decelerator that could be deployed at either supersonic or hypersonic speeds and is able to bring heavier payloads to the destination planet²². However, IAD development has not yet reached the maturity and Technology Readiness Level to be implemented into future space missions. Additional research and developments are required to advance IAD technologies. Several national agencies currently are working on IAD developments including the Air Force²³, DARPA²⁴, European Space Agency²⁵, and NASA²⁶⁻³⁰. The most recent HIAD flight tests have been performed at NASA Langley Research Center. The first of these tests was the Inflatable Reentry Vehicle Experiment (IRVE) in September, 2007 however it failed to deploy due to rocket failure. The follow-on mission, IRVE-II, was launched on a Black Brant XI sounding rocket from NASA's Wallops Flight Facility in 2009. IRVE-II employed a 3-meter diameter, 60° half-angle configuration consisting of seven tori, laced together and arranged into three separate inflatable volumes³¹. The article initiated descent supersonically at an altitude of 211 km and the inflatable heat-shield was deployed within 90 seconds at an altitude of 200 km³². This flight experiment successfully demonstrated many aspects required of inflatable technologies including exo-atmospheric inflation, inflatable structure performance, flexible thermal protection systems, aerodynamic stability, and structural integrity during atmospheric entry. On July 23rd, 2012, IRVE-III was launched from NASA's Wallops Flight Facility. It had a different configuration than IRVE-II but same diameter. This project further demonstrated the potential capability of the HIAD technology including the use of a center of gravity offset to generate lift as well as providing higher peak heating to test the Thermal Protection System (TPS) capabilities.

In order for HIADs to be considered for future missions there must be confidence in their ability to perform successfully as an entry device in the conditions in which they will be flown. Given that limitations of ground-test facilities prevent full scale testing, this entails ensuring that they perform successfully during wind tunnel and flight-testing and that those test results can be correlated to relevant flight regimes to predict their capabilities under those environments. Analyzing such test data for stability and drag performance allows for characterization of HIAD performance as a drag device under the flight relevant conditions. In addition, transferring this data to flight regimes outside of those being tested requires confidence in the models being used to describe the HIAD and the ability of these models to capture the relevant physics both within and outside the test conditions. This investigation focuses on estimating the inflated shape and dynamics of a 6m 60-degree half-angle sphere cone HIAD test article under a range of loading conditions.

II. Ground Test Campaign

The HIAD configuration is composed of two major components: a rigid center-body made of Aluminum and several tori composed of fiber reinforced thin films. Kevlar straps hold the tori together. In addition, the HIAD investigated has an aerodynamic skin cover that mimics the structure of a flexible TPS.³³ Two configurations were tested, seen in Fig. 1. The Baseline configuration is composed of seven structural tori (T_1 - T_7) and one shoulder torus (T_8). The second configuration, called the Tri-tori, builds upon the Baseline configuration by adding an additional torus located between T_6 and T_7 ($T_{6.5}$) (also seen in Fig. 1 in the red circle) and was developed to investigate whether this addition substantially improved rigidity.

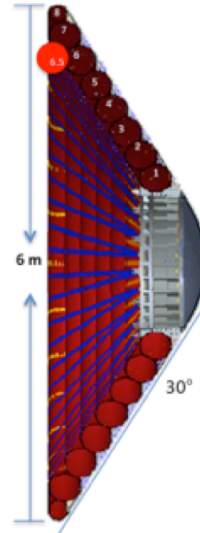


Figure 1. Cross-sectional view of the HIAD structure

Testing of a subscale 6m diameter HIAD was conducted in the 40 by 80 foot wind tunnel at NASA Ames Research Center with the HIAD mounted on a sting. In the wind tunnel, four pairs of stereoscopic camera systems were mounted in the center, lower, and upper sections of the East wall as well as on the floor and ceiling.³³ The set-up was chosen to provide a full view of the HIAD and to permit 3D tracking. This is shown in Fig. 2. Each camera acquired data at 15 Hz for 10 seconds producing 150 frames for each dataset and was synched by a signal pulse from the facility data acquisition system. Camera placement was determined before testing by using virtual imaging software in order to meet the design and resource constraints in the wind tunnel environment.³⁴ Photogrammetry software (ARAMIS) was used to generate the full 3D model and the photogrammetry data obtained from each camera pair was stitched together with SVIEW.

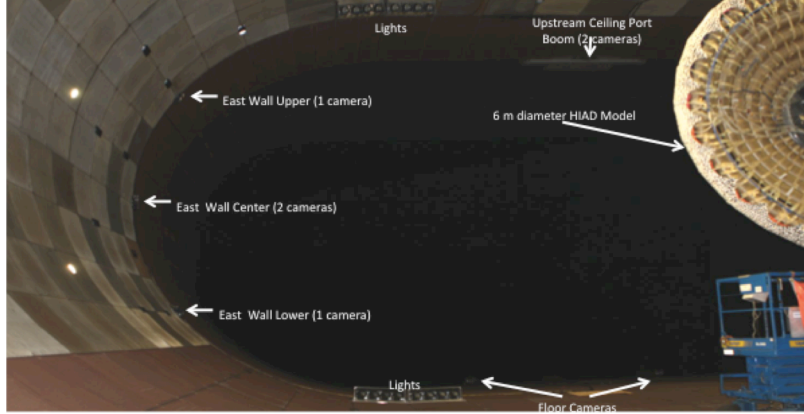


Figure 2. Photogrammetry camera setup

In order to develop a deflection data set sufficient to validate aero-elastic models, three parameters were studied: yaw angle, free-stream dynamic pressure, and inflation pressure. The test matrix can be seen in Table 1.

Table 1. Test matrix

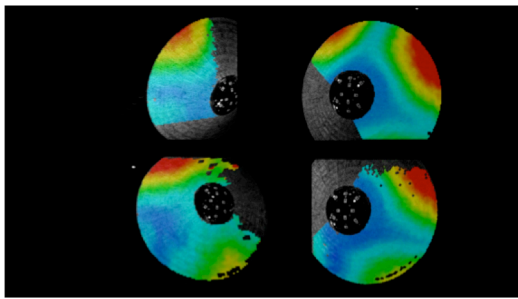
Yaw Angle (deg)	Dynamic Pressure (psf)	Inflation Pressure (psi)	
-25, -15, -5, 0, 5, 10	8, 40, 50, 65, 70	I_2	15 (all tori)
		I_3	10 ($T_{3-6,8}$), 15 ($T_{1,2,7}$)
		I_4	8 (T_{3-6}), 15 ($T_{1,2,7}$)

The yaw angle was modulated to simulate an angle of attack during actual flight. Positive yaw angles were defined as a clockwise rotation when looking down upon the wind tunnel. Dynamic pressure was changed by adjusting the freestream air velocity. The maximum wind tunnel dynamic pressure was limited to 70 psf by NFAC safe operating procedures. The last parameter analyzed was the inflation pressure of the individual tori. Three settings were used to investigate the sensitivity of the HIAD stiffness to inflation pressure.³³

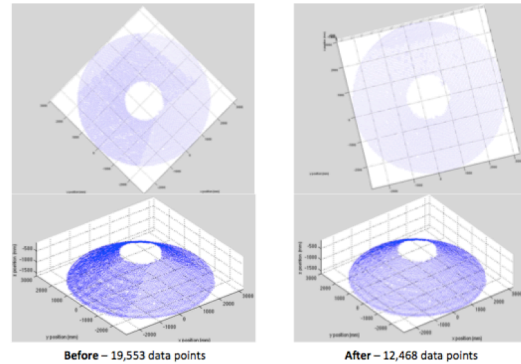
III. Methodology and Results

A. Photogrammetry Data Uniqueness

The photogrammetry measurements are used to determine the aeroshell shape and deformation under the range of test parameters.³¹ A full 3D HIAD model was constructed by combining data obtained from at least two camera-pairs. Figure 3a shows an example of the data captured by the four different stereoscopic camera-pairs during a run. The data in this figure is represented by colors while gray is an area of no information. When multiple views are



(a) Images from separate camera pairs taken from ARAMIS



(b) HIAD model before and after data cleanup

Figure 3. Photogrammetry stitching and data cleanup

stitched together to create the full model, overlapping sections contain redundant information increasing the computational cost when performing data analysis. A MATLAB script was written to delete the overlapping data. A comparison of data files before and after running the MATLAB script showed that the resulting files were approximately 60% of their original size. Depiction of the photogrammetry data before and after the clean-up can be seen in Fig. 3b.

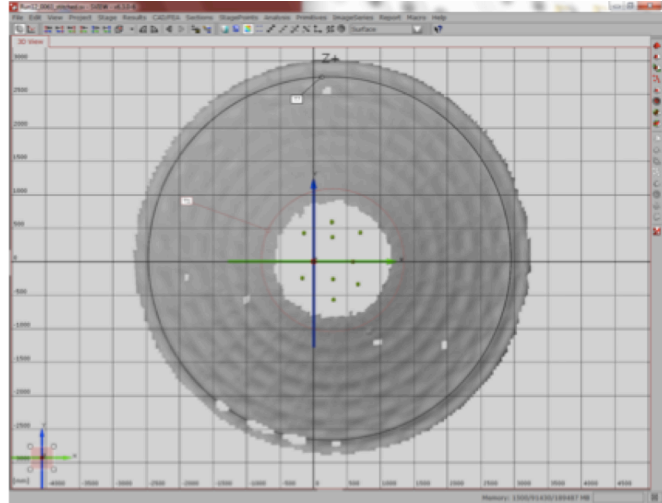
B. Deflection Angle Measurements

One use of the photogrammetry data was to have quick feedback of the HIAD behavior in a wind tunnel environment before performing higher fidelity analysis. For consistency, the deflection angle was calculated based on the location of the peaks of tori T_1 and T_7 . Given the symmetry of the problem, it was of interest to calculate the deflection angle at four radial directions: 0° (up, N), 90° (right, E), 180° (down, S), and 270° (left, W). (The yaw plane is aligned with the 90° and 270° directions). Much like exporting the full 3D HIAD model from the photogrammetry software, the data along the peaks of T_1 and T_7 could also be exported individually. This was done by selecting three points on the desired peak, which would generate a circle of data that could be exported. This process is shown in Fig. 4a.

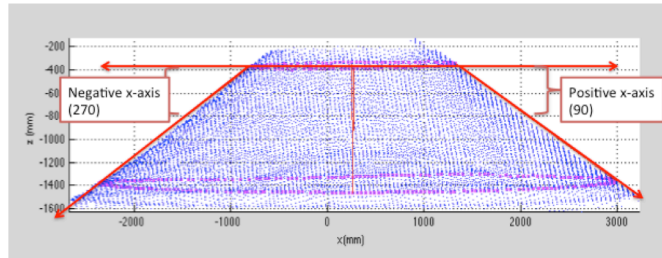
A MATLAB routine was developed to compute the deflection angles. The code finds the points on tori T_1 and T_7 corresponding to the 0° , 90° , 180° , and 270° radial directions. These points were used to create vectors and the resulting vectors were used to calculate the deflected angle of the HIAD in each direction. This process can be seen in Fig. 4b. These angles could then be compared to the no wind case and the difference used to infer the loaded deformation. By analyzing deformation over various dynamic pressures, yaw angles, and inflation settings, system trends were established regarding HIAD performance.

An overall comparison was performed that looked at the deflection of the Baseline and Tri-tori configurations over all available data sets. In this way, average performance of both configurations could be assessed. The deflection angles for the Baseline and Tri-Tori configurations under all available test conditions and for each radial direction (0, 90, 180 and 270 degrees) are plotted together in Fig. 5. It can be seen that both the Baseline and Tri-Tori configurations have deflection angles between 0 and 5 degrees. However, the Baseline configuration has one point that had a deflection angle of around 8.5 degrees, seen in Fig. 5a. Since there are no other deflection angles near this value (even when considering the other radial direction of that same run) it was decided that this point was an outlier, likely due to the inaccuracy of determining the peak of T_1 and T_7 or due to rapid oscillations for that case. Therefore, it was discarded in Fig. 5b.

Table 2 displays the deflection angle statistics for data shown in Fig. 5 for both the Baseline and Tri-Tori configurations. When looking at the average of all cases it can be seen that the Baseline and Tri-Tori configuration have, on average, a deflected angle of 2 degrees. When accounting for the standard deviation in these results, the deflection angles of the Baseline and Tri-Tori are each in the range of 1 to 3 degrees. Therefore, we can conclude that the Tri-Tori configuration does not provide a substantial increase in rigidity when compared to the Baseline configuration. As evidenced by the mean and median values, both HIAD configurations are fairly rigid.

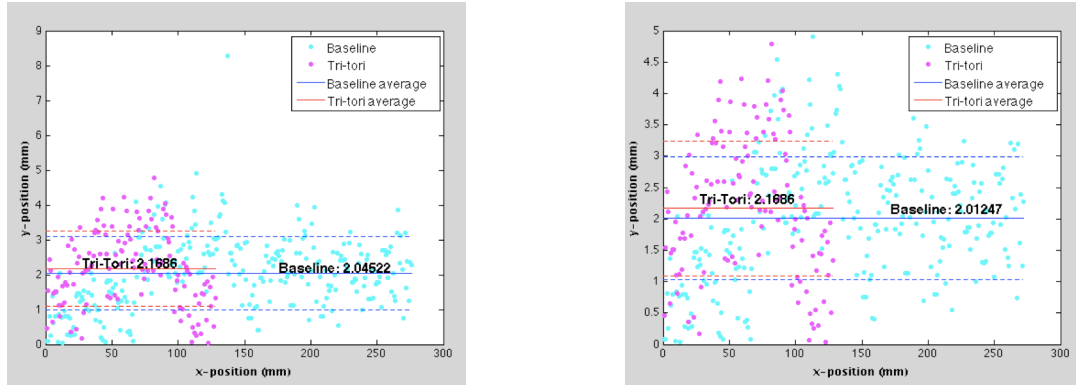


(a) Exporting T_1 and T_7 from the photogrammetry software



(b) Vectors used to calculate the deflected angle

Figure 4. Visualization of deflected angle calculations



(a) All deflected angle results (b) All deflected angle results (without outlier point)

Figure 5. All deflected angle results with statistics

Table 2. Summary of all deflected angle results

	Baseline	Tri-tori	% Difference (compared to baseline)
Average Deflection	2.01	2.17	7.80%
Standard Deviation	0.98	1.08	10.20%
Max Deflection	4.91	4.79	-2.44%
Median Deflection	2.02	2.15	6.44%

The uncertainty of the calculations presented here are unknown at this time since the error in the cameras, calibration, and imaging are not included. For a better understanding of the Baseline and Tri-Tori performance, error bars can be included to understand the certainty of the results. The error bars for both configurations are assumed to be the same since the same photogrammetry system was used for each. For this first order analysis, the standard deviation values were provided to indicate the variation across all trials.

C. Averaging Routine

There were large errors between deflection angles calculated from different frames of photogrammetry data due to the HIAD oscillations during testing. These errors clouded trends in the data and motivated the use of a single data set that was representative of all 150 frames. Thus, a MATLAB script was created to average the data points among all of the frames. When the photogrammetry software outputs the 3D coordinates of a point on the HIAD surface it also provides a unique set of indices for that point that can identify it in each frame of data. An example of point coordinates and indices can be seen in Fig. 6. The MATLAB script first saves all of the points to a file and sorts them by their indices, grouping points with like identity indices. It then iterates through each set of identity indices and averages the resulting set of 3D positions to produce an averaged position. The average is calculated using equation 1 taking into account the total number of frames that contain the given point.

Point Indices			Point Coordinates		
x-index	y-index	sub-index	x	y	z
135	22	0	142.25	3006.74	-1443.57
136	22	0	187.44	3004.81	-1430.71
137	22	0	235.38	3002.06	-1420.90
138	22	0	285.21	2999.04	-1413.27
139	22	0	335.71	2995.60	-1406.32
140	22	0	388.40	2991.61	-1401.47
141	22	0	441.31	2987.70	-1396.74
142	22	0	495.35	2983.67	-1393.02

Figure 6. 3D position of photogrammetry points including the identity matrix

$$x_{ave} = \frac{1}{N} \sum_{i=1}^n x_i; y_{ave} = \frac{1}{N} \sum_{i=1}^n y_i; z_{ave} = \frac{1}{N} \sum_{i=1}^n z_i \quad (1)$$

In cases where the photogrammetry does not identify a point in one or more frames, these frames do not contribute to that point's averaged position since the MATLAB routine cannot find the point's identifier. The script stores the averaged position of every point as the averaged data set and outputs the data to a file for use in future analysis.

D. Standard Deviation to Estimate HIAD Oscillations

It was shown that oscillation of the HIAD caused significant deviations between different frames of a single test run. To quantify the average response of the HIAD as well as estimate the oscillatory motion, the standard deviation in position among all 150 frames of a single run was calculated. Regions of high standard deviation indicate significant motion while regions of low standard deviation indicate limited motion. In addition, localized regions of high standard deviation may indicate a structural defect or other phenomena. The standard deviation of each point about its mean location was calculated via Eq. 2.

$$\sigma_x = \sqrt{\frac{1}{N} \sum_{i=1}^N (x_i - x_{ave})^2}; \sigma_y = \sqrt{\frac{1}{N} \sum_{i=1}^N (y_i - y_{ave})^2}; \sigma_z = \sqrt{\frac{1}{N} \sum_{i=1}^N (z_i - z_{ave})^2} \quad (2)$$

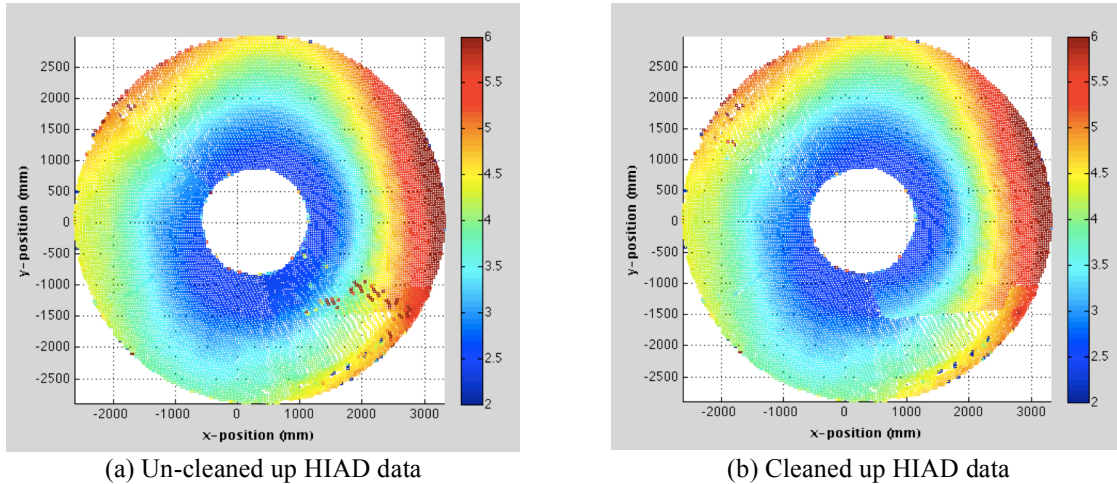
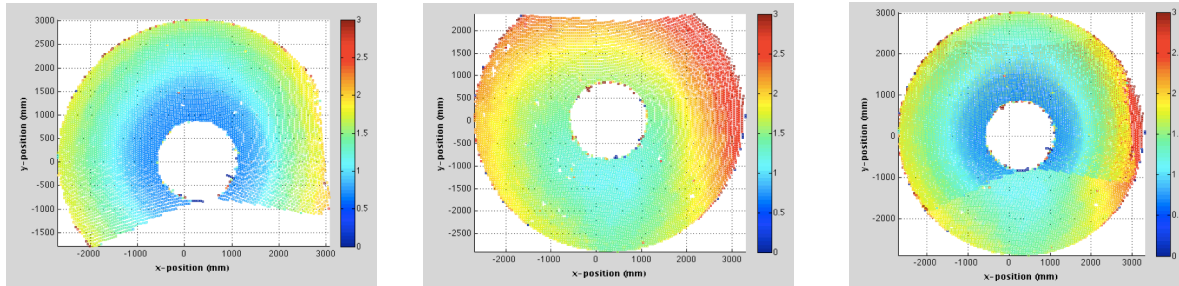


Figure 7. Standard deviation in the absolute position of all point on the HIAD (70 psf, -25° yaw angle, I_3 inflation setting)

Figure 7 shows a top down view the HIAD depicting the standard deviation in the absolute position of each point. This run was performed at 70 psf with a -25° yaw angle and I_3 inflation setting. Two observations can be made from the graphs. The first observation is that there is a small cluster of high deviation points along the 135° radial direction (southeast direction) in Fig. 7a. Since these points are on the interface of the two different camera pairs, they are likely artifacts created from stitching together the different views and do not have physical significance. The points were removed after running the MATLAB data clean-up script.

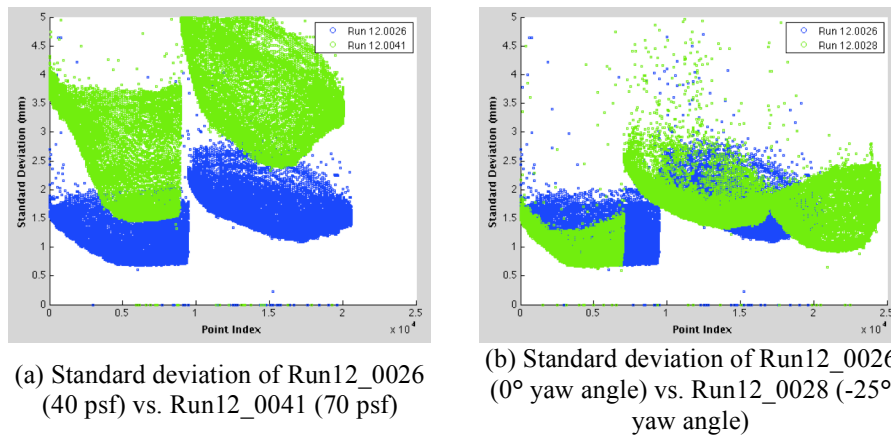
The second observation is that the standard deviation in position increases when moving radially outward from the center but is not radially uniform across the entire HIAD. If the HIAD were a rigid oscillator, the points on the perimeter would have more motion than points near the center and would thus have a higher standard deviation in their position. This is apparent in Fig. 7. However, the standard deviation would be symmetric about the y -axis with highest standard deviation occurring along the yaw plane ($y = 0$). In this case, there is a distinct difference between the lower left and upper right portions of the graph. In particular, across the interface of the two data sets (along the 135° and 315° radial directions) a noticeable change in positional standard deviation can be seen. These two regions correspond to imaging of the HIAD from different camera pairs. The fact that they do not observe the same deviation at their interface is concerning since it shows that each camera pair does not capture the same motion of the HIAD. The lower left camera pair sees high deviation along the 135° and 315° radial directions while the upper right camera pair sees very high deviation along the 90° radial direction.

This phenomenon is also seen in a different run, tested at 40 psf with a 0° yaw angle and I_3 inflation setting. As seen in Fig. 8, the standard deviation in position observed from the top camera pair is much lower than that observed from the bottom pair. When the two views are stitched together (shown in Fig. 8c), the datasets are simply overlaid. Therefore, in the overlapping region, the datasets predict that points right next to each other would have significantly different standard deviations and possible different mean deflections. This is not physically possible and shows that the differences in the standard deviation predicted by each camera pair distort the trends in the overall datasets. It is not clear from this analysis which data set is more accurate but further analysis will be performed to investigate why cameras are not observing the same motion.



(a) View from top camera pair (b) View from bottom camera pair (c) View of overlapping datasets
Figure 8. Standard deviation of HIAD photogrammetry data including views from each individual camera pair (40 psf, 0° yaw angle, I_3 inflation setting)

It is also important to investigate how sensitive the positional standard deviation of each point is to the different test parameters. Figure 9a shows the standard deviation results for two runs conducted at different dynamic pressures while Fig. 9b shows the results from two runs conducted with different yaw angles. These graphs illustrate the overall standard deviation for a particular set of test conditions. The shape of each graph is not important since the points are plotted without regards to their order nor is the number of points important since it is dependent on the number and viewing angles of the camera pairs, neither of which are important to this discussion. From Fig. 9a, it is evident that positional standard deviation increases with increasing dynamic pressure. This makes physical sense that there would be more HIAD motion with increased flow velocity. This was also observed qualitatively during testing. From Fig. 9b, no substantial change in the positional standard deviation is evident with yaw angle. This also makes physical sense. While motion would likely increase on one side of the HIAD, this would likely be counteracted by reduce motion on the other.

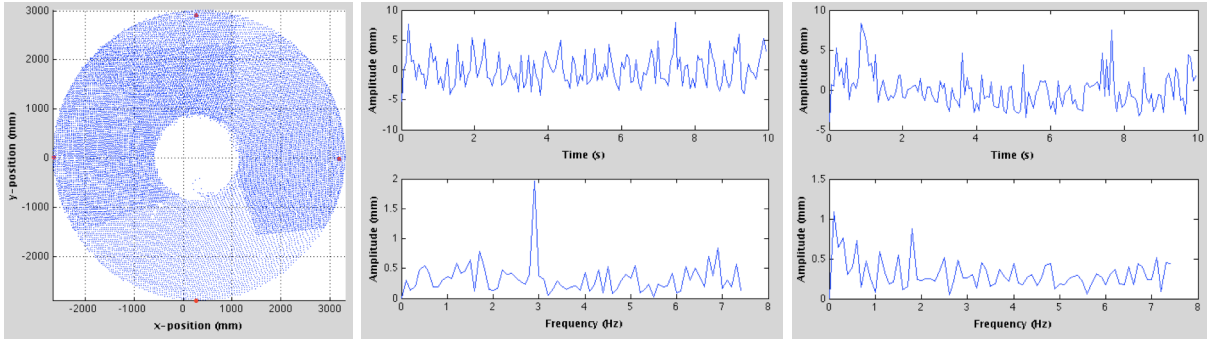


(a) Standard deviation of Run12_0026 (40 psf) vs. Run12_0041 (70 psf) (b) Standard deviation of Run12_0026 (0° yaw angle) vs. Run12_0028 (-25° yaw angle)
Figure 9. Standard deviation comparisons between different dynamic pressures and yaw angles

E. Oscillation Frequency to Predict External Forcing

There is significant interest in describing the oscillations that were observed during testing to understand the HIAD dynamics and infer its stability. Given that the HIAD is a blunt body it was hypothesized that oscillations would result from vortex shedding. Thus, the frequency of oscillation was investigated in order to determine if the frequency of motion correlated to the vortex shedding frequency around the HIAD and if not, if the frequency of motion could be attributed to another known source.

A frequency analysis was performed on a single point using its position data over time. For each run, 4 points were chosen along each of the 0° , 90° , 180° and 270° radial directions. The locations of these points are shown in Fig. 10a as red dots. In this way, motion at different frequencies could be isolated and analyzed to see if there were trends with inflation setting, yaw angle or free-stream dynamic pressure. For each point, a Discrete Fast Fourier Transform was taken of its position over the 150 frames (over time) to determine the frequency content of its motion. Frequencies with the highest amplitudes corresponded to the dominant modes of motion. Figures 10b and 10c show the time signal and FFT for the points along the 90° and 270° radial directions for a run with an I_3 inflation setting, dynamic pressure of 70 psf and -25° yaw angle.



(a) Points chosen for FFT

(b) Signal and FFT for total motion of a single point in 90° radial direction

(c) Signal and FFT for total motion of a single point in 270° radial direction

Figure 10. Motion in the time and frequency domains for select points on the HIAD

It is necessary to perform an FFT of the amplitude vs. time graphs (top of Figs. 10b and 910c) to determine frequency content since the motion is chaotic. However, even the FFT graphs do not show a clear overall trend. An ideal FFT would show spikes at a few dominant forcing frequencies with zero amplitude signals everywhere else. Since noise is always present, it would show in the FFT graph as a band of low but relatively constant amplitude data spanning the entire frequency range. Figure 10b shows a promising graph with a very high amplitude peak at 2.9 Hz and moderately low noise surrounding it. However, when looking at Fig. 10c, no dominant peak is seen at all. Thus, it is unclear whether the frequency content of the motion is able to resolve different forcing functions acting on the HIAD. When derived via another method, the vortex shedding was calculated to be 6 Hz. It is natural that a blunt body such as a HIAD in a uniform free stream would experience dominant forcing from vortex shedding around the body so the fact that this wasn't resolved in the motion is concerning.

The photogrammetry cameras sampled data at 15 Hz. In order for a Discrete Fourier Transform to avoid aliasing of a signal the sampling frequency must be at least 2 times the highest frequency of that signal.^{35,36} It is uncertain whether or not 15 Hz was large enough to meet this criterion since the highest frequency of oscillation is not known. Given this problem and the poor results that were observed (analysis performed on other runs gave similar conclusions) it seems as though this method is unable to resolve the HIAD forcing using the current photogrammetry setup. While the method has promise, other data sources with higher sampling frequencies are necessary to derive useable conclusions.

F. Oscillation Frequency to Analyze HIAD Motion

Even though the FFT method did not resolve specific forcing frequencies it still provides insight into the HIAD oscillations. Two analyses were performed to estimate the rigidity of the HIAD: 1. along a single radial direction and 2. azimuthally along a constant radius circle. Rigidity was determined based on all points moving cohesively, evidenced by them each having the same frequency content of motion.

The rigidity of the HIAD along each radial direction was investigated by taking the FFT of the position history for multiple points along a single radial direction (both on the peaks of each torus as well as in between tori). Figure 11 shows the FFT results along the 0° radial direction ($+y$ direction) for a run conducted at 70 psf, yaw angle of 0° and I_3 inflation setting. Figure 11a plots the distance away from the nose versus the frequency content of motion. Marker size and color is determined by the amplitude of the signal at that frequency (as determined by the FFT). A distinct high frequency peak at around 3 Hz is found in each plot and smaller peaks are also observed. All peaks in the FFT graphs align and all graphs are the same shape (seen in the vertical lines spanning Fig. 11a). This shows that each point along the radial direction acts cohesively and oscillates at the same frequency. Figure 11b also depicts the oscillation frequency versus distance away from the nose (x and y -axes, respectively), and includes the amplitude of motion at each frequency on the z -axis. The peak frequencies at each distance away from the nose all align.

Furthermore, the amplitude increases while moving outwards from the nose cone so points on the outer tori have greater displacement than points on inner tori. As a result, movement along a single radial direction behaves like a rigid rod constrained by the aluminum nose cone.

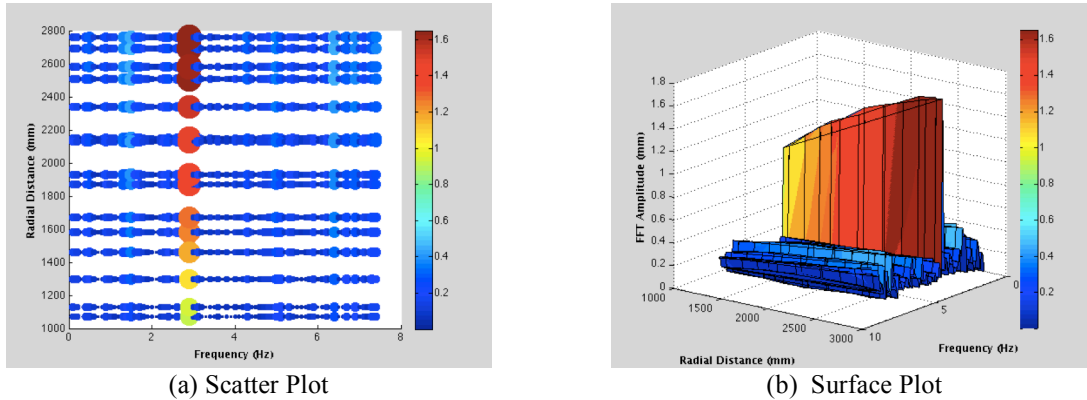


Figure 11. Frequency content of motion along the 0° radial direction (70 psf, -25° yaw angle, I_3 inflation setting)

The rigidity of the HIAD along azimuthal directions was investigated by selecting 20 points distributed uniformly, all 2.5m away from the center (seen in Fig. 12a). Diagrams are shown for a run conducted at 70 psf, 0° yaw angle and I_3 inflation setting. The scatter plot depicts the frequency content of motion for each radial direction plotted in a polar graph with low frequencies towards the center and higher frequencies found radially outward (Fig. 12b). Higher amplitude signals are shown via colors and larger markers. The surface plot also shows frequency content of motion versus azimuthal angle (x and y -axes, respectively) and includes signal amplitude on the z -axis (Fig. 12c).

The surface plot shows a continuous valley between 35° and 250° , which is to be expected if the HIAD were a rigid cone oscillating about the pitch plane. There are also large, discontinuous jumps in oscillation amplitude at 20° , 280° and 340° showing that the HIAD is not rigid at these locations. However, discontinuous motion was not observed during wind tunnel testing so this analysis was expected to produce a continuous frequency graph. When comparing Figs. 12a and 12b, the locations of the discontinuities match with where the camera pair views overlap (denoted by intensity of color in Fig. 12a). Therefore, the FFT graphs are continuous for individual camera pairs, but discontinuous in overlapping regions. This was the same result seen from the standard deviation analysis and highlights deficiencies in stitching the camera views together.

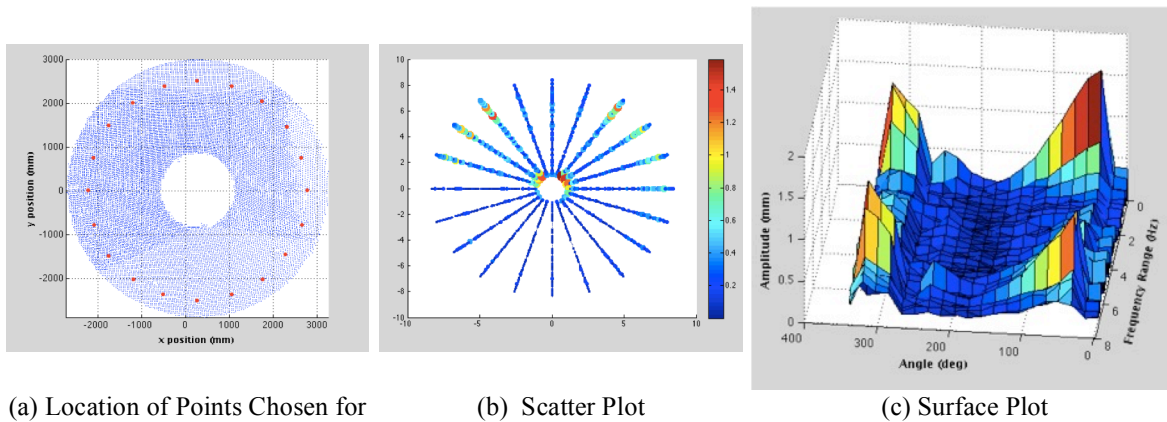


Figure 12. Frequency content of motion when traveling azimuthally, 2.5m from the HIAD nose (70 psf, 0° yaw angle, I_3 inflation setting)

IV. Summary

Many avenues have been explored to analyze HIAD static and dynamic characteristics while under different loading conditions, including deflection angle measurements as well as calculating the standard deviation of the deformed shape and frequency response quantification. The deflection angle results show that, on average, static

deflection increases with dynamic pressure but is insensitive to yaw angle (equivalent to angle of attack). Calculations of the standard deviation about the mean deflection show that motion of the HIAD increases while moving radially outwards and that motion was significantly higher in the yaw plane. It was seen that the standard deviation also increases with increasing dynamic pressure, but is relatively constant with yaw angle. Observing the positional standard deviation of the points along the entire HIAD showed that different camera pairs did not observe the same motion and calculated different standard deviations at their interface. The frequency analysis showed that high frame-rate photogrammetry is necessary to predict external forcing on the HIAD to avoid aliasing of higher frequency signals. Frequency analysis also showed that the frequency content of motion was continuous along a single radial direction. The amplitude of motion increases when moving radially outward showing that each radial direction behaves similar to a rigid rod constrained at one end by the center-body. In addition, the frequency content of motion was continuous azimuthally for each camera pair. However, motion calculated from different camera pairs was not cohesive, especially at their interface. These discontinuities were observed in both the frequency and standard deviation analyses, due to the method of stitching together data from separate camera pairs.

V. Acknowledgments

The authors would like to thank NASA who funded the work discussed here as part of the Master Thesis Project. Collaboration with Calvin Tran who made Fig. 3a, Fig.4a, and exported the photogrammetry data is also greatly appreciated. Special thanks to Dr. Pauken who diligently reviewed this paper and provided great feedback.

VI. References

- ¹ Braun, R. D. and Manning, R. M., "Mars Exploration Entry, Descent, and Landing Challenges," *Journal of Spacecraft and Rockets*, Vol. 44, No. 2, 2007, pp. 310 –323.
- ² Atlas V Launch Services User's Guide". Centennial, CO: United Launch Alliance. 2010-03. Retrieved 2011-12-04.
- ³ Gold, D., "Early Development of the Manually Operated Personnel Parachute, 1900-1919," Proceedings of the DOD/AIAA Aerodynamic Deceleration Systems Conference, edited by E. C. Myers, Air Force Flight Test Center, Edwards Air Force Base, Calif., FTC-TR-69-11, Vol. II, April 1969, pp. 403-416.
- ⁴ Hillje, Ernest R., "Entry Aerodynamics at Lunar Return Conditions Obtained from the Flight of Apollo 4 (AS-501)," NASA TN D-5399, (1969)
- ⁵ Knacke, T. W., "The Apollo Parachute Landing System," Proceedings of the DOD/AIAA Aerodynamic Deceleration Systems Conference, edited by E. C. Myers, Air Force Flight Test Center, Edwards Air Force Base, Calif., FTC-TR-69-11, Vol. II, April 1969, pp. 329-338.
- ⁶ Kiker, J. W., "The Apollo Recovery System," presented at Deutsche Gesellschaft fur Luft-und Raumfahrt E. V., Deutsche Forschungs-und Versuchsanstalt, and Advisory Group for Aerospace Research and Development Symposium on Aerodynamic Deceleration, Technical University of Braunschweig, West Germany, Sept. 15-19, 1969
- ⁷ Way, D. W., et al, "Mars Science Laboratory: Entry, Descent, and Landing System Performance," IEEE Aerospace Conference, Big Sky, MT, March 3-10, 2006.
- ⁸ Cruz, J.R., Lingard, J.S., "Aerodynamic Decelerators for Planetary Exploration: Past, Present, and Future," AIAA Guidance, Navigation, and Control Conference and Exhibit, AIAA 2006-6792, August 2006.
- ⁹ Leonard, R.W., Brooks, G.W., McComb Jr., H.G., "Structural Considerations of Inflatable Reentry Vehicles," NASA Technical Note, NASA TN-D-457, September 1960.
- ¹⁰ Charzenko, N., McSheara, J.T., "Aerodynamic Characteristics of Towed Cones Used as Decelerators at Mach numbers from 1.57 to 4.65," NASA Technical Note, NASA TN-D-994, December 1961.
- ¹¹ Alexander, W.C., "Investigation to Determine the Feasibility of Using Inflatable Balloon Type Drag Devices for Recovery Applications in the Transonic, Supersonic, and Hypersonic Flight Regime Part II: Mach 4 to Mach 10 Feasibility Investigation," Flight Accessories Laboratory Technical Report, ASD TDR 62-702, December 1962.
- ¹² Charzenko, N., "Aerodynamic Characteristics of Towed Spheres, Conical Rings, and Cones Used as Decelerators at Mach Numbers from 1.57 to 4.65, NASA Technical Note, NASA TN-D-1789, April 1963.
- ¹³ Deitering, J.S., Hilliard, E.E., "Wind Tunnel Investigation of Flexible Aerodynamic Decelerator Characteristics at Mach Numbers 1.5 to 6.0," ARO Inc. Technical Report, AEDC TDR-65-110, June 1965.
- ¹⁴ Kyser, A.C., "Deployment Mechanics for an Inflatable Tension-Cone Decelerator," NASA Contractor Report, NASA CR-929, November 1967.
- ¹⁵ Reichenau, D.E.A., "Investigation of an Attached Inflatable Decelerator System for Drag Augmentation of the Voyager Entry Capsule at Supersonic Speeds," ARO Inc. Technical Report, AEDC TR-68-71, April 1968.
- ¹⁶ Baker, D.C., "Investigation of an Inflatable Decelerator Attached to a 120-deg Conical Entry Capsule at Mach

- Numbers from 2.55 to 4.40,” ARO Inc. Technical Report, AEDC TR-68-227, October 1968.
- ¹⁷ Bohon, H.L., Miserentino, R., “Attached Inflatable Decelerator (AID) Performance Evaluation and Mission-Application Study,” *Journal of Spacecraft*, Vol. 8, No. 9, September 1971.
 - ¹⁸ Creel, T.R., Miserentino, R., “Aerodynamic Heating at Mach 8 of Attached Inflatable Decelerator Configurations,” NASA Technical Memorandum, NASA TM-X-2355, October 1971.
 - ¹⁹ Willis, C.M., Mikulas Jr., M.M., “Static Structural Tests of a 1.5-Meter-Diameter Fabric Attached Inflatable Decelerator,” NASA Technical Note, NASA TN-D-6929, October 1972.
 - ²⁰ Nebiker, F.R., “Development of a Ballute Recovery System for Mach 10 Flight and Its Practical Applications,” Goodyear Aerospace Corporation Contractor Report, GER-11467A, August 1964.
 - ²¹ Fallon II, E.J., “Supersonic Stabilization and Deceleration: Ballutes Revisited,” AIAA 95-1584-CP, 1995.
 - ²² Cianciolo, A. D., et al, “Overview Of The NASA Entry, Descent and Landing Systems Analysis Exploration Feed-Forward Study,” International Planetary Probe Workshop, 2011.
 - ²³ Graham, W.A., “MK 82 Ballute Retarder System Updated for Advanced Weapons Program,” 16th Aerodynamic Decelerator Systems Technology Conference and Seminar, AIAA 2001-2039, May 2001.
 - ²⁴ Iannotta, B. “Future Mars Craft Inspires High-Tech Spy Plane,” Space.com Online Publication, Posted 31 October 2007.
 - ²⁵ Walther, S. et al., “New Space Application Opportunities based on the Inflatable Reentry & Descent Technology (IRDT),” AIAA/ICAS International Air and Space Symposium and Exposition: The Next 100 Years, AIAA 2003-2839, July 2003.
 - ²⁶ Miller, K.L., Gulick, D., Lewis, J., Trochman, B., Stein, J., Lyons, D.T., Wilmoth, R.G., “Trailing Ballute Aerocapture: Concept and Feasibility Assessment,” 39th AIAA/ASME/SAE/ASEE Joint Propulsion Conference and Exhibit, AIAA 2003-4655.
 - ²⁷ Hughes, S.J., Dillman, R.A., Starr, B.R., Stephan, R.A., Lindell, M.C., Player, C.J., Cheatwood, F.M., “Inflatable Re-entry Vehicle Experiment (IRVE) Design Overview,” 18th AIAA Aerodynamic Decelerator Systems Technology Conference and Seminar, AIAA 2005-1636, September 2005.
 - ²⁸ Richardson, E.H., Munk, M.M., James, B.F., Moon, S.A., “Review of NASA In-Space Propulsion Technology Program Inflatable Decelerator Investments,” 18th AIAA Aerodynamic Decelerator Systems Technology Conference and Seminar, AIAA 2005-1603, July 2005.
 - ²⁹ Masciarelli, J.P., Lin, J.K.H., Ware, J.S., Rohrschneider, R.R., Braun, R.D., Bartels, R.E., Moses, R.W., Hall, J.L., “Ultra Lightweight Ballutes for Return to Earth from the Moon,” 47th AIAA/ASME/ASCE/AHS/ASC Structures, Structural Dynamics, and Materials Conference, AIAA 2006-1698, May 2006.
 - ³⁰ Player, C., “Inflatable Aerodynamic Decelerators Technology Development,” Fundamental Aeronautics 2007 Annual Meeting Conference Proceedings, October 2007.
 - ³¹ Lindell, M. C., Hughes, S. J., Dixon, M., and Willey, C. E. (2006). “Structural Analysis and Testing of the Inflatable Re-entry Vehicle Experiment (IRVE),” AIAA Paper AIAA 2006-1699, 47th AIAA/ASCE/AHS/ASC Structures, Structural Dynamics, and Materials Conference, Newport, RI, May 1-4, 2006.
 - ³² NASA Launches New Technology: An Inflatable Heat Shield, NASA Mission News, 2009-08-17, accessed 2011-01-02.
 - ³³ Cassell, A.M., Swanson, G.T., Johnson, R.K., Hughes, S.J., and Cheatwood, F.M.. “Overview of the Hypersonic Inflatable Aerodynamic Decelerator Large Article Ground Test Campaign,” 21st AIAA Aerodynamic Decelerator Systems Technology Conference and Seminar, May, 2011.
 - ³⁴ Kushner, L.K., Schairer, E.T., “Planning Image-Based Measurements in Wind Tunnels by Virtual Imaging,” 49th AIAA Aerospace Sciences Meeting, AIAA 2011-930, Orlando, FL.
 - ³⁵ Nyquist, Harry. "Certain factors affecting telegraph speed". *Bell System Technical Journal*, 3, 324–346, 1924
 - ³⁶ Nyquist, Harry. "Certain topics in telegraph transmission theory", *Trans. AIEE*, vol. 47, pp. 617–644, Apr. 1928